

# Investigating the hyperparameter space of deep neural network models for reaction coordinates

Kawashima, Kyohei

Institute for Materials Chemistry and Engineering, Kyushu University

Sato, Takumi

Department of Interdisciplinary Engineering Sciences, Interdisciplinary Graduate School of Engineering Sciences, Kyushu University

Okazaki, Kei-ichi

Research Center for Computational Science, Institute for Molecular Science

Kim, Kang

Division of Chemical Engineering, Department of Materials Engineering Science, Graduate School of Engineering Science, Osaka University

他

<https://hdl.handle.net/2324/7347418>

---

出版情報 : APL Machine Learning. 3 (1), 2025-03-13. AIP Publishing







バージョン :

権利関係 : © 2025 Author(s).



RESEARCH ARTICLE | MARCH 13 2025

## Investigating the hyperparameter space of deep neural network models for reaction coordinates

Kyohei Kawashima ; Takumi Sato; Kei-ichi Okazaki ; Kang Kim ; Nobuyuki Matubayasi ; Toshifumi Mori  



*APL Mach. Learn.* 3, 016113 (2025)

<https://doi.org/10.1063/5.0252631>



View  
Online



Export  
Citation

### Articles You May Be Interested In

Effect of data preprocessing and machine learning hyperparameters on mass spectrometry imaging models

*J. Vac. Sci. Technol. A* (September 2023)

Hyperparameter optimization for autoencoders that perform content-based image retrieval

*AIP Conf. Proc.* (December 2019)

Hyperparameter tuning for malaria detection using convolution neural network

*AIP Conf. Proc.* (June 2024)



## Special Topics Open for Submissions

[Learn More](#)





# Investigating the hyperparameter space of deep neural network models for reaction coordinates

Cite as: APL Mach. Learn. 3, 016113 (2025); doi: 10.1063/5.0252631

Submitted: 11 December 2024 • Accepted: 11 February 2025 •

Published Online: 13 March 2025



Kyohei Kawashima,<sup>1</sup>  Takumi Sato,<sup>2</sup> Kei-ichi Okazaki,<sup>3,4,a)</sup>  Kang Kim,<sup>5,b)</sup>  Nobuyuki Matubayasi,<sup>5,c)</sup>   
and Toshifumi Mori<sup>1,2,d)</sup> 

## AFFILIATIONS

<sup>1</sup> Institute for Materials Chemistry and Engineering, Kyushu University, Kasuga, Fukuoka 816-8580, Japan

<sup>2</sup> Department of Interdisciplinary Engineering Sciences, Interdisciplinary Graduate School of Engineering Sciences, Kyushu University, Kasuga, Fukuoka 816-8580, Japan

<sup>3</sup> Research Center for Computational Science, Institute for Molecular Science, Okazaki, Aichi 444-8585, Japan

<sup>4</sup> Graduate Institute for Advanced Studies, SOKENDAI, Okazaki, Aichi 444-8585, Japan

<sup>5</sup> Division of Chemical Engineering, Department of Materials Engineering Science, Graduate School of Engineering Science, Osaka University, Toyonaka, Osaka 560-8531, Japan

<sup>a)</sup> Electronic mail: keokazaki@ims.ac.jp

<sup>b)</sup> Electronic mail: kk@cheng.es.osaka-u.ac.jp

<sup>c)</sup> Electronic mail: nobuyuki@cheng.es.osaka-u.ac.jp

<sup>d)</sup> Author to whom correspondence should be addressed: toshi\_mori@cm.kyushu-u.ac.jp

## ABSTRACT

Identifying reaction coordinates (RCs) is a key to understanding the mechanism of reactions in complex systems. Deep neural network (DNN) and machine learning approaches have become a powerful tool to find the RC. On the other hand, the hyperparameters that determine the DNN model structure can be highly flexible and are often selected intuitively and in a non-trivial and tedious manner. Furthermore, how the hyperparameter choice affects the RC quality remains obscure. Here, we explore the hyperparameter space by developing the hyperparameter tuning approach for the DNN model for RC and investigate how the parameter set affects the RC quality. The DNN model is built to predict the committor along the RC from various collective variables by minimizing the cross-entropy function; the hyperparameters are automatically determined using the Bayesian optimization method. The approach is applied to study the isomerization of alanine dipeptide in vacuum and in water, and the features that characterize the RC are extracted using the explainable AI (XAI) tools. The results show that the DNN models with diverse structures can describe the RC with similar accuracy, and furthermore, the features analyzed by XAI are highly similar. This indicates that the hyperparameter space is multimodal. The electrostatic potential from the solvent to the hydrogen H<sub>18</sub> plays an important role in the RC in water. The current study shows that the structure of the DNN models can be rather flexible, while the suitably optimized models share the same features; therefore, a common mechanism from the RC can be extracted.

© 2025 Author(s). All article content, except where otherwise noted, is licensed under a Creative Commons Attribution (CC BY) license (<https://creativecommons.org/licenses/by/4.0/>). <https://doi.org/10.1063/5.0252631>

## I. INTRODUCTION

The transition state (TS) plays a fundamental role in chemical reactions and enzyme catalysis.<sup>1–5</sup> While reactions in a simple model system can be well characterized using a few TSs, the reactions in solution and biomolecules involve numerous intermediates and TSs on the high-dimensional potential energy surface.<sup>6–10</sup> It is thus indispensable to describe the reactions on the low-dimensional free energy surface (FES) described by a few collective variables (CVs),

and it has been of great interest to determine the optimal CVs from a number of possible CV candidates that can adequately describe the FES and TS. In a representative case of alanine dipeptide, the conformational transitions have been successfully characterized with the FES using two dihedral angles,  $\phi$  and  $\psi$ , known as the Ramachandran plot<sup>11</sup> (Fig. 1).

From a kinetic perspective, TS is considered a point in the potential or free energy surface having an equal probability of reaching the reactant and product states.<sup>12–14</sup> The committor  $p_B(\mathbf{x})$ ,

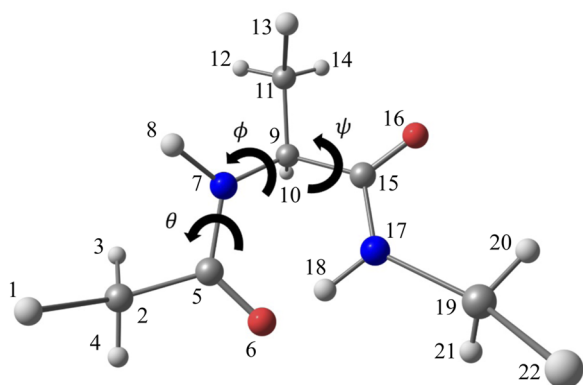


**FIG. 1.** Alanine dipeptide with atom indices. The three key dihedral angles, i.e.,  $\phi$ ,  $\psi$ , and  $\theta$ , the dihedral angles about the  $C_5-N_7$ ,  $N_7-C_9$ , and  $C_9-C_{15}$  bonds, respectively, are also shown. Dihedral angles used in the text are expressed in degrees.

defined as the probability of reaching the state  $B$  from the configuration denoted by  $\mathbf{x}$  without returning to state  $A$ , changes monotonically from 0 to 1 along an ideal RC and becomes 0.5 at the TS.  $p_B$  thus serves as a good measure to evaluate the quality of a RC and have been used to optimize the RCs from a large number of candidate CVs.<sup>15–29</sup> These studies of RCs have led to the realization that an adequate RC that satisfies the  $p_B \sim 0.5$  condition is often much more complicated than typical CVs used to build the FESs.<sup>17,22,30</sup> For instance, in the case of alanine dipeptide, the  $C_{eq}-C_{ax}$  transition in vacuum required another dihedral angle  $\theta$  (Fig. 1),<sup>15</sup> and the reaction in water is even more complex and challenging.<sup>15,17</sup> In particular, the RC in water has only been characterized successfully with an elaborated reaction coordinate, i.e., the solvent-derived electrostatic torque around one of the main-chain bonds, showing the challenge in identifying the RC coordinate when the solvent is present.<sup>17</sup>

Machine learning (ML) approaches have recently been actively applied to identify the CVs and RCs from the molecular dynamics (MD) simulation trajectories.<sup>19,31–50</sup> In particular, Ma and Dinner<sup>17</sup> have developed an automatic CV search algorithm by combining the genetic algorithm to identify the RC for the alanine dipeptide isomerization. Along this line, we have recently combined the deep neural network (DNN) approach with the cross-entropy minimization method<sup>24,25</sup> to optimize the RC from many CV candidates using the committor distribution as a measure.<sup>43,51</sup> Our study highlighted the effectiveness of the explainable AI (XAI) method in characterizing the CVs that contribute to the RC.

While the DNN approach can be very powerful in describing the non-linear contributions of CVs to RC, the structure of the DNN model, characterized by the hyperparameters, e.g., the number of layers and nodes per layer, is highly flexible and is often chosen intuitively. Yet, the adequacy of the hyperparameters remains ambiguous. In this regard, Neumann and Schwierz<sup>44</sup> have recently applied the Keras Tuner random search hyperparameter optimization to automatically determine the DNN model that can describe the committor of the magnesium binding to RNA. Nevertheless, how the choice of hyperparameters affects the quality of the DNN model and the outcome remains unclear. The applications of

DNN models thus suffer from determining the appropriate hyperparameters, which remains to be a highly tedious and non-trivial task.

In this work, we developed a hyperparameter tuning protocol that utilizes the Bayesian optimization method with a Gaussian process<sup>52</sup> to determine the DNN model for RC optimization. The method takes the committors and a large number of candidate CVs as the input without pre-determined hyperparameters for the DNN model and automatically determines the appropriate DNN model for the RC. The RC for the isomerization of alanine dipeptide in vacuum and in water is studied. The diversity in the optimized hyperparameters and its effect on the RCs are explored, and the character of the RC for each model is analyzed by applying the XAI methods. Furthermore, we show that the reaction in solution can be characterized using a more straightforward set of CVs while the complexity in the RC can be taken into account through the DNN framework.

## II. METHODS

### A. Committor and cross entropy function

Committor  $p_B(\mathbf{x})$  describes the probability of a trajectory generated from  $\mathbf{x}$  to reach the product state  $B$ . Along a RC  $q$ ,  $p_B$  is expected to change smoothly from 0 to 1 and become 0.5 at the transition state. The ideal committor value at  $q$ ,  $f_B(q)$ , can thus be described by a sigmoidal function,  $f_B(q) = (1 + \tanh(q))/2$ .

When the data point  $k$  is characterized by the collective variables (CVs)  $\mathbf{x}^{(k)}$  and committor  $p_B^{(k)}$ , the discrepancy between the ideal value and raw committor data can be described by the cross-entropy function,<sup>24,25</sup>

$$\mathcal{H}(q) = -\sum_k p_B^{(k)} \log f_B(q^{(k)}) - \sum_k (1 - p_B^{(k)}) \log \{1 - f_B(q^{(k)})\}, \quad (1)$$

where  $k$  denotes the data points and  $q^{(k)}$  is the RC as a function of  $\mathbf{x}^{(k)}$ . Equation (1) is derived from the Kullback–Leibler divergence,<sup>24</sup> which quantifies the mismatch between the distribution of the raw ( $p_B^{(k)}$ ) and expected ( $f_B(q^{(k)})$ ) committors. It is also noted that Eq. (1) is a generalization of the maximum-likelihood function used with the aimless shooting algorithm.<sup>18</sup>

By minimizing Eq. (1), one can optimize  $q^{(k)}$  to minimize the difference between  $p_B$  and  $f_B(q^{(k)})$ . In practice, we employ the  $L_2$  regularization function to suppress overfitting and, therefore, the loss function is defined as a sum of  $\mathcal{H}$  and the penalty term.<sup>24</sup> The regularization parameter  $\lambda$  is set separately for each layer (see below).

### B. Deep neural network model

The DNN function converts the CVs  $\mathbf{x}^{(k)}$  into a RC  $q^{(k)}$  in a non-linear manner. Here, we adopt the multilayer perceptron model, which consists of the input layer  $\mathbf{x}^{(k)}$ , multiple hidden layers with different numbers of nodes, and the output layer  $q^{(k)}$  (Fig. 2). The CVs are standardized prior to constructing  $\mathbf{x}^{(k)}$ . The leaky rectified linear unit (Leaky ReLU) with a leaky parameter set of 0.01 was used for the activation function. The  $L_2$  regularization was employed, where  $\lambda$  was varied in the hyperparameter tuning step. Note that different  $\lambda$  was used for each layer. The numbers of hidden layers and nodes

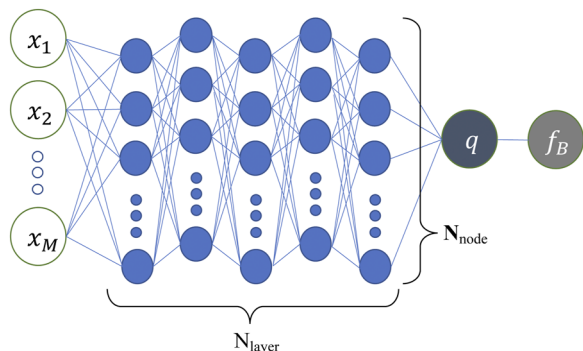


**FIG. 2.** Overview of the multilayer perceptron model used in this work. The input CVs ( $x_i$ ) are converted to the output ( $q$ ) with a DNN model of  $N_{\text{layer}}$  consisting of  $N_{\text{node}}$ .  $f_B$  is the predicted  $p_B$  value at  $q$  described by a sigmoidal function ( $f_B(q) = (1 + \tanh(q))/2$ ).

in each layer,  $N_{\text{layer}}$  and  $N_{\text{node}}$ , respectively, are also the hyperparameters that are left to be explored. Optimization was performed using AdaMax. The learning rate  $lr$  and two decay factors  $\beta_1$  and  $\beta_2$  were set to the default values of 0.001, 0.9, and 0.99, respectively. The TensorFlow<sup>53</sup> library was used to implement the DNN model.

### C. Hyperparameter tuning and DNN model optimization

The hyperparameters in the current DNN,  $N_{\text{layer}}$ ,  $N_{\text{node}}$ , and  $\lambda$ , are not unique and can strongly affect the performance of the DNN model. Here, we employ the hyperparameter tuning approach using the Bayesian optimization method with a Gaussian process<sup>52</sup> to determine these parameters in an automatic manner.

The hyperparameter tuning and DNN model optimization are performed in two stages. First, the data are divided into a training and validation set at a ratio of 8:2.  $N_{\text{layer}}$  is searched between 2 and 5, and  $N_{\text{node}}$  are explored separately for each layer, which are chosen within the range from 100 to 5000 in 100 increments.  $\lambda$  is explored between 0.0001 and 0.100 with 20 points equally spaced in a logarithmic scale. The initial values for these parameters are chosen randomly within the exploration range. Bayesian optimization was performed for 150 trials unless otherwise noted, where the DNN model for each hyperparameter was trained for a maximum of 1000 epochs using Eq. (1). Early stopping was applied when the value of the loss function for the validation set did not improve for five consecutive steps. The performance of the model at each step was evaluated using the root-mean-square error (RMSE) for the validation set, calculated as a difference between the predicted and reference  $p_B$ . After the optimal choice of the parameters is determined, the data are unified and re-partitioned into training, validation, and test sets at a ratio of 5:1:4, and the DNN model is optimized for 1000 epochs with the same criteria for early stopping. The Keras Tuner<sup>54</sup> library was used to implement the hyperparameter tuning with a Gaussian process.

### D. DNN model interpretation with LIME and SHAP

To interpret the DNN model, the Local Interpretable Model-agnostic Explanation (LIME)<sup>55</sup> and SHapley Additive exPlanations

(SHAP)<sup>56</sup> methods were applied to the data. In brief, LIME builds a linear regression function to explain the local behavior of the target data from the perturbation of input variables, whereas SHAP employs an additive feature attribution method that ensures fair distribution of predictions among input features in accordance with the game-theory-based Shapley value. LimeTabularExplainer for LIME and DeepExplainer for SHAP were employed, using the packages obtained from <https://github.com/marcotcr/lime> and <https://github.com/slundberg/shap>, respectively.

### E. Conformational sampling of alanine dipeptide

The initial structures of alanine dipeptide in vacuum and water were generated using AmberTools21.<sup>57</sup> In the case of water, alanine dipeptide was solvated in a rectangular parallelepiped box with 1683 water molecules. Alanine dipeptide and water were treated with the Amber14SB force field and TIP3P model, respectively. The system was energy minimized for 3000 steps and heated up to 300 K in 50 ps. MD simulations under NPT and NVT conditions were then performed for 100 and 1000 ps, respectively, to complete equilibration.

Umbrella sampling (US) and transition path sampling (TPS) were combined to collect broad conformations about the transition path of alanine dipeptide in vacuum and water as follows: First, the transition state region (i.e.,  $\phi \sim 0$ ) was sampled using the US along  $\phi$  with a force constant of 100.0 kcal mol<sup>-1</sup> rad<sup>-2</sup> while restraining  $\psi - \psi \leq 0$  with a half-harmonic potential with a force constant of 10.0 kcal mol<sup>-1</sup> rad<sup>-2</sup> (see Fig. 1 for definitions of  $\phi$  and  $\psi$ ). 100 conformations from the 10 ns-long trajectory with the harmonic restraint centered at  $\phi = 0.0$  were then evenly collected. From each conformation, ten trajectories of 2 ps long were generated by sampling the initial velocity from the Maxwell-Boltzmann distribution at 300 K and propagating the trajectory for 1 ps forward and backward in time under the NVE condition. States A and B were defined as  $\phi \leq -30$  and  $\phi \geq 30$ , respectively. It is noted that while the previous studies<sup>15,17</sup> have often studied the  $C_{7eq} \rightarrow \alpha_R$  transitions in solution, which have lower energy barriers,<sup>58</sup> here we focus on the isomerization about  $\phi$  to compare the results in vacuum and water.

From the successful transition trajectories that connect states A and B, new points were generated by extracting snapshots within 0.1 ps from the time origin of each trajectory. The velocity for each point was sampled from the Maxwell-Boltzmann distribution at 300 K, and a new ensemble of 2 ps-long trajectories was generated following the same procedure as above. Roughly 33% and 42% of the trial trajectories were accepted throughout the TPS of alanine dipeptide in vacuum and water, respectively. After the 3rd round, 3714 and 4590 points were generated for the following committor calculations in vacuum and in water.

From each data point after the final round of TPS, 2 ps-long trajectories were generated 100 times per point with velocities randomly sampled from the Maxwell-Boltzmann distribution at 300 K.  $p_B$  was calculated by  $p_B = n_B / (n_A + n_B)$ , where  $n_I$  denotes the number of trajectories that are at state  $I$  at the end of the trajectory. The data points projected on the  $(\phi, \psi)$  plane, with colors describing the  $p_B$  value, are shown in Fig. 3. We note that the data points were obtained over a broader range of  $\phi$  compared to those sampled with



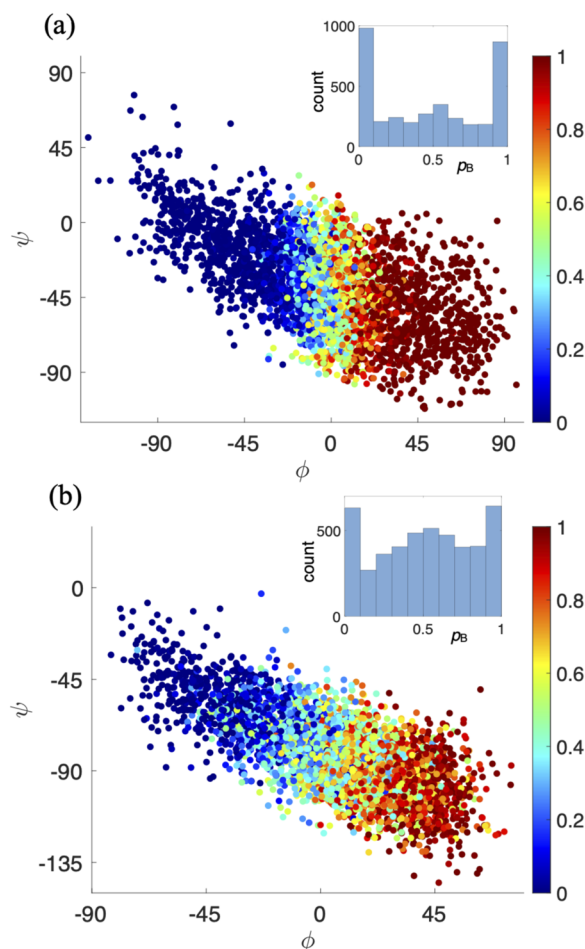


**FIG. 3.** Distributions of the data points in  $(\phi, \psi)$  space from the trajectories in (a) vacuum and (b) water. Colors represent the calculated  $p_B$  data at each point. The insets in (a) and (b) show the committor distributions for all the data points in vacuum and water, respectively.

the aimless shooting algorithm.<sup>25</sup> As a consequence, the  $p_B$  distributions were not even, especially in a vacuum, where roughly half of the points were found in either  $p_B \leq 0.1$  or  $p_B \geq 0.9$ . Here we note that the minima on the  $\phi < 0$  side in water, corresponding to the  $\alpha_R$  state, is located at  $\psi < 0$ .<sup>17,58</sup> The transition path in water is thus also located on the  $\psi < 0$  side compared to that in a vacuum.

The collective variables (CVs) are listed in [supplementary material](#), Table S1, and the atom indices are given in [Fig. 1](#). All MD simulations were performed using the Amber 20 software package.<sup>57,59</sup>

### III. RESULTS AND DISCUSSION

#### A. Convergence of optimal hyperparameters

We first compare the results of hyperparameter tuning for the isomerization of alanine dipeptide in a vacuum. Ten models were

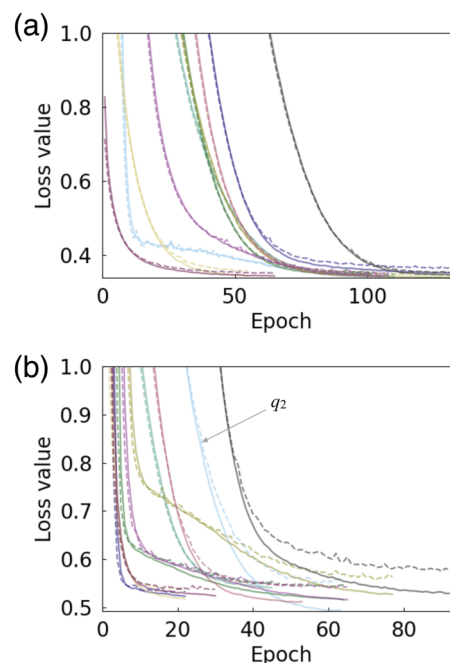


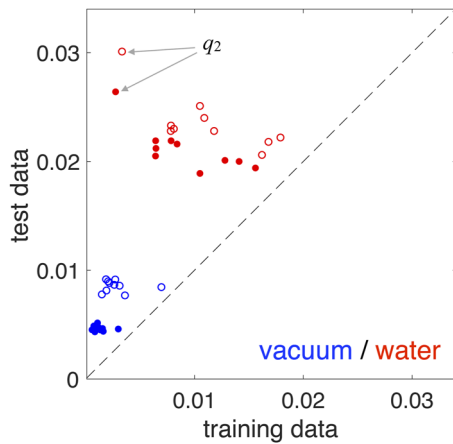
**FIG. 4.** Training process of the loss function as a sum of the cross-entropy function and the  $L_2$  regularization term in (a) vacuum and (b) water. Full and dashed lines show the values for training and validation data along the training process, and colors denote results for different models. Note that the training and datasets in each model are different due to different initial seeds for data partitioning.

constructed using different initial seeds, including data partitioning. The CV candidates consist of 45 dihedral angles in cosine and sine forms, i.e., 90 variables, which follow our previous studies.<sup>25,43</sup> The convergence of the loss function, given in [Fig. 4](#), shows that the optimizations are converged within 60–100 epochs. Since further extending the number of epochs leads to a slightly decreased loss function for the training data but an increase in that for the validation data, we find that these epoch numbers are sufficient for suppressing overfitting and maximizing predictability. The obtained hyperparameters are summarized in [Table I](#). Surprisingly, the number of layers ( $N_{\text{layer}}$ ) and nodes ( $N_{\text{node}}$ ) differ remarkably between the models.  $N_{\text{node}}$  often converged to the maximum (5000) or to the minimum (100), and  $N_{\text{node}} = 5$  was most frequently selected (5 out of 10 models).  $\lambda$  was often found to be at the minimum (0.0001), especially in the first layer, but can be up to 0.0695 and varied between the layers. We note that before converging to these values, different regions of the hyperparameter space have been explored before converging to the optimal values in each model ([Fig. S1](#)). Overall, no apparent unique optimal model was obtained.

To compare the accuracy of the coordinates from the perspective of  $p_B$ -predictability, the RMSE between the predicted and reference  $p_B$  for the training and test data are shown in [Fig. 5](#) for the ten models. The RMSEs were within 0.005 and around 0.005 for the training and test sets, respectively. Even the RMSEs for the data points about the TS ( $-0.2 < q_i < 0.2$ ) are within 0.007 and 0.009 for the training and test data. These results indicate that while

**TABLE I.** Optimized hyperparameters in vacuum.  $q_i$  denotes the RC obtained for the  $i$ th model.

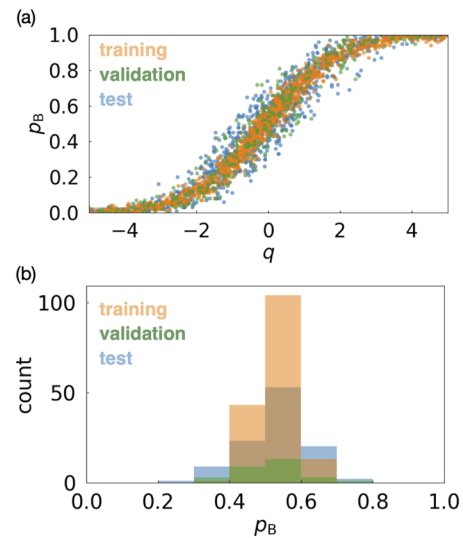
	$q_1$	$q_2$	$q_3$	$q_4$	$q_5$	$q_6$	$q_7$	$q_8$	$q_9$	$q_{10}$
$N_{\text{layer}}$	5	2	3	5	5	3	5	4	2	5
$N_{\text{node}}^{(1)}$	5000	4000	4000	3500	5000	1400	5000	4100	2700	5000
$\lambda^{(1)}$	0.0001	0.0001	0.0001	0.1000	0.0001	0.0001	0.0001	0.0009	0.0001	0.0001
$N_{\text{node}}^{(2)}$	5000	5000	2500	5000	5000	5000	5000	2700	100	2100
$\lambda^{(2)}$	0.0001	0.0113	0.0026	0.0001	0.1000	0.0001	0.0013	0.0018	0.0009	0.1000
$N_{\text{node}}^{(3)}$	5000	...	2900	100	4300	100	5000	3600	...	5000
$\lambda^{(3)}$	0.0695	...	0.0001	0.0001	0.0001	0.0001	0.0001	0.0006	...	0.0026
$N_{\text{node}}^{(4)}$	3600	...	...	2400	100	...	5000	900	...	100
$\lambda^{(4)}$	0.1000	...	...	0.0002	0.0001	...	0.1000	0.0002	...	0.0001
$N_{\text{node}}^{(5)}$	100	...	...	5000	5000	...	2000	...	...	5000
$\lambda^{(5)}$	0.0001	...	...	0.0001	0.0001	...	0.0001	...	...	0.0001

**FIG. 5.** Scatter plot for RMSEs between the predicted and reference  $p_B$  for the training and test datasets. Filled and open circles indicate the RMSEs using full points and those at about the TS ( $-0.2 < q_i < 0.2$ ), respectively. Blue and red colors are the results in vacuum and water.

the optimized DNN models are not unique, the RCs show very similar quality, i.e., able to predict  $p_B$  with similar accuracy. This implies that the hyperparameter space for the current DNN model is likely multimodal.

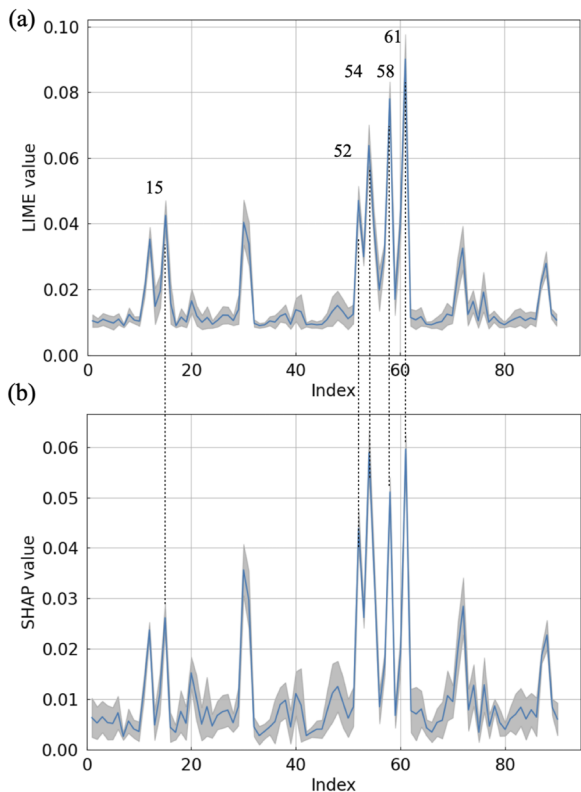
Figure 6 summarizes the change of  $p_B$  along the first RC ( $q_1$ ). Figure 6(a) shows that both training and test data closely follow the ideal sigmoidal line. The histogram of  $p_B$  about the transition state [Fig. 6(b)] indicates that both the training and test datasets show a sharp peak at  $p_B \sim 0.5$ . These results imply that  $q_1$  serves as a good RC and can clearly characterize the transition state. We note that similar results are obtained for the other RCs (Figs. S2 and S3).

Figure 7 summarizes the features that contribute to RC at about the TS extracted from LIME and SHAP. The extracted features are found to be very similar between the ten RCs.  $CV_{61}$ ,  $CV_{58}$ , and  $CV_{54}$ , corresponding to the sine form of  $\phi$ ,  $\phi$ , and  $\theta$ , respectively, are the three major CVs in LIME analysis. The contribution of  $\theta$  is increased in the SHAP analysis, but the key CVs are unchanged from

**FIG. 6.** (a) Scatter plots of the optimized coordinate ( $q$ ) and committor ( $p_B$ ) for  $q_1$  in vacuum. (b) Distribution of  $p_B$  for the points within  $-0.2 < q_1 < 0.2$ . Orange, green, and blue in (a) and (b) denote the results from the training, validation, and test datasets, respectively.

those found in LIME. The result is consistent with the previous studies, which showed that  $\theta$  becomes important at about the transition state.<sup>17,25,43</sup> On the other hand, the order as well as the magnitude of the contributions are slightly different from those obtained in the previous XAI analysis.<sup>43</sup> This may be due to the differences in the distribution of the data points, where the current points are distributed over a broader range along  $\phi$  (Fig. 3).

We also directly compared the RCs obtained from different DNN models in the scatter plots and correlation coefficients (Fig. S4). The result shows that every pair of RCs is highly correlated, and the correlation coefficient is  $>0.99$ , indicating that despite the difference in the hyperparameters, the obtained RCs are very similar. It is noted that the points at the negative and positive ends of the



**FIG. 7.** Contributions of CVs to the RCs in vacuum extracted using (a) LIME and (b) SHAP in absolute values. Blue lines and gray shades denote the average and variance calculated from the ten RCs.

RCs, where  $p_B$  is 0 and 1, respectively, show slight deviations from the diagonal line in some of the plots. This is because  $p_B$  is insensitive to the changes in the RCs at these ranges and, therefore, these points are not further optimized. The current results show that while the optimization of DNN hyperparameters does not lead to a unique

model, each DNN model produces equally accurate RCs with similar predictability of  $p_B$  and common features that describe the TS.

**B. Characterization of solvation coordinates using DNN**

Next, we apply the current approach to the isomerization of alanine dipeptide in water. Compared to the case in a vacuum, the reaction in water has been a challenging task due to the contribution from the numerous waters surrounding the solute.<sup>15</sup> Previously, a complex CV involving the solvent-derived electrostatic torque has been proposed to be important for the  $C_{7eq} \rightarrow \alpha_R$  transition.<sup>17</sup> Here, we attempt to adopt more intuitive CVs to describe the solvent contribution and account for the complex non-linear contribution through the DNN model. To this end, the electrostatic and van der Waals interactions from the waters to the atoms in the alanine dipeptide were used as the CVs in addition to the internal coordinates of the alanine dipeptide (i.e., dihedral angles). Optimizations of the hyperparameters and DNN models were performed in the same manner as those in vacuum.

As is the case in a vacuum, the optimized DNN models for the RCs in water were found to converge to different parameter sets (Table II).  $N_{layer} = 3$  most frequently appeared, and  $N_{node}$  was on average slightly smaller than those in vacuum. For instance, in the case of  $q_1$ , the hyperparameter space was found to be explored quickly before converging to the optimal value (Fig. S5); the larger number of layers was explored, but only for a short period in  $q_1$ ; in the latter exploration stage, the  $N_{layer} = 3$  was most intensely searched, and  $N_{layer}$  of 3 was found to be optimal. On the other hand,  $\lambda$  was found to become larger than those in a vacuum. These trends indicate that the increase in the number of CVs in water resulted in a slightly more compact model but with a higher regularization penalty to suppress overfitting.

The RMSEs between the calculated and reference  $p_B$ s, plotted in Fig. 5, show that the RMSEs for the training data are mostly distributed between 0.006 and 0.015 whereas those for the test data are found at around 0.02. Only in one case do we find a slight sign of overfitting, where the RMSE for the training and test data are 0.002 and 0.026, respectively. The RMSEs for the data about the transition

**TABLE II.** Optimized hyperparameters in water.  $q_i$  denotes the RC obtained for the  $i$ th model.

	$q_1$	$q_2$	$q_3$	$q_4$	$q_5$	$q_6$	$q_7$	$q_8$	$q_9$	$q_{10}$
$N_{layer}$	3	5	3	3	5	2	3	2	3	5
$N_{node}^{(1)}$	100	4400	3800	2900	5000	1700	1300	2900	2300	5000
$\lambda^{(1)}$	0.0001	0.0004	0.0013	0.0001	0.0001	0.0026	0.0009	0.0018	0.0001	0.0001
$N_{node}^{(2)}$	1200	1700	1600	5000	5000	100	800	100	5000	5000
$\lambda^{(2)}$	0.1000	0.0162	0.0483	0.0079	0.0079	0.0018	0.1000	0.0234	0.0483	0.0055
$N_{node}^{(3)}$	3100	3800	1400	100	2000	...	3000	...	400	2500
$\lambda^{(3)}$	0.0055	0.0004	0.0336	0.1000	0.1000	...	0.0018	...	0.0234	0.1000
$N_{node}^{(4)}$	...	800	...	...	5000	...	...	...	...	2000
$\lambda^{(4)}$	...	0.0003	...	...	0.1000	...	...	...	...	0.1000
$N_{node}^{(5)}$	...	600	...	...	100	...	...	...	...	3700
$\lambda^{(5)}$	...	0.0009	...	...	0.0001	...	...	...	...	0.0055



state ( $-0.2 < q_i < 0.2$ ) show a similar trend. These results indicate that while the RMSEs for the data in water are larger than those in a vacuum for both the training and test data, the optimized RCs can satisfactorily predict  $p_B$ s.

The change of  $p_B$  along  $q_1$  in water is summarized in Fig. 8. The results for other RCs are illustrated in Figs. S6 and S7. The distribution of  $p_B$  [Fig. 8(a)] is broader than the case in a vacuum but follows a sigmoidal curve as a function of  $q_1$ . The histogram of  $p_B$  near the TS [Fig. 8(b)] shows a peak at  $p_B \sim 0.5$  with the width of the histograms broader than those in vacuum. The results for the other optimized coordinates in Fig. S6 are mostly consistent with  $q_1$ . We note that only in the case of  $q_2$ , the histogram for the training data is sharply peaked while that for the test data is broad, implying that overfitting to the training data has occurred. This is consistent with the loss function values and RMSE results [Figs. 4(b) and 5(b), respectively].

Figure 9 shows the contributions of CVs to the RCs at about the TS extracted by LIME and SHAP. Note that these analyses include  $q_2$ , because excluding  $q_2$  only slightly changed the result (Fig. S8). Similarly to the case in vacuum,  $CV_{61}$ ,  $CV_{58}$ , and  $CV_{54}$ , corresponding to  $\phi$ ,  $\phi$ , and  $\theta$ , respectively, are found to be the three major CVs. Apart from these three CVs,  $CV_{125}$ , the electrostatic potential from the water on  $H_{18}$  ( $V_{\text{ele}}(H_{18})$ ) (Fig. 1), shows up as a key feature from the solvent. In addition,  $CV_{105}$  and  $CV_{119}$ , which are the electrostatic potential on  $H_8$  and  $C_{15}$ , respectively, show notable contributions to the RC. The same trend is found in the SHAP result, though the relative balance is somewhat changed. The scatter plots of  $V_{\text{ele}}(H_{18})$  and  $\phi$  or  $\theta$ , given in Figs. 10(a) and 10(b), respectively, do not show a clear correlation between the changes of CVs and  $p_B$  or any apparent separatrix. On the other hand, the plot as a function of the three variables [Fig. 10(c)] shows that there is a weak correlation between  $V_{\text{ele}}(H_{18})$  and  $p_B$  near the separatrix in the  $(\phi, \theta)$  space. Therefore, the solvation coordinate  $V_{\text{ele}}(H_{18})$  is contributing to the RC in a

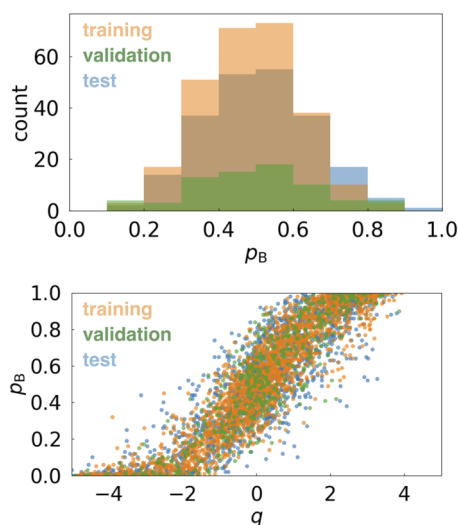


**FIG. 8.** (a) Scatter plots of the optimized coordinate ( $q$ ) and committor ( $p_B$ ) for  $q_1$  in water. (b) Distribution of  $p_B$  for the points within  $-0.2 < q_1 < 0.2$ . Orange, green, and blue in (a) and (b) denote the results from the training, validation, and test datasets, respectively.

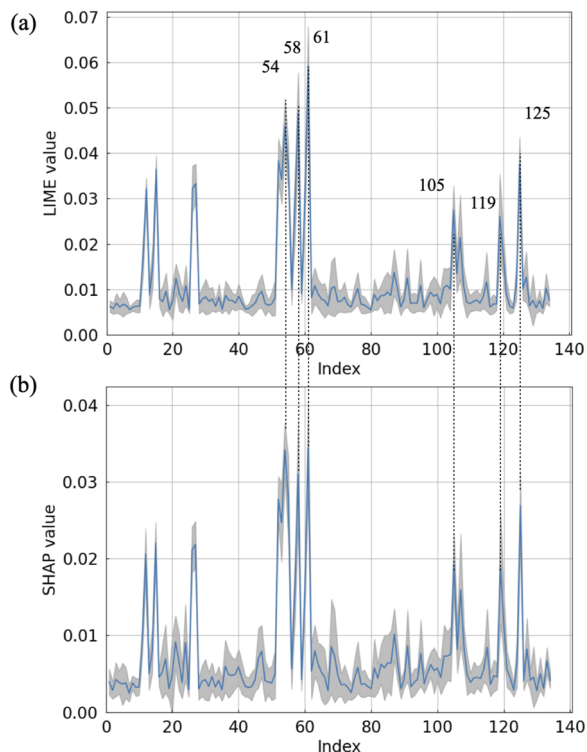


**FIG. 9.** Contributions of CVs to the RCs in water extracted using (a) LIME and (b) SHAP in absolute values. Blue lines and gray shades denote the average and variance calculated from the ten RCs.

nontrivial manner. Interestingly, the importance of the solvent effect on  $H_{18}$  has also been indicated by Ma and Dinner<sup>17</sup> for the  $C_{7\text{eq}} \rightleftharpoons \alpha_R$  transition through the torque coordinate as mentioned earlier. The structures about the TS for  $q_1$  are also summarized in Fig. S11. The figure shows that the position of  $H_{18}$  strongly depends on  $\psi$ , which ranges between  $-123 < \psi < -50$ . A water molecule is frequently placed near  $H_{18}$  but without clear orientation. This confirms that the solvent contributes to the reaction coordinate in a collective manner.

Finally, the RCs in water are directly compared in Fig. S9. Compared to the vacuum results (Fig. S4), the deviation from the diagonal line is slightly larger even at  $q_i \sim 0$  (i.e., near TS). Nevertheless, the overall correlation between the RCs is very high and found to be above 0.96, except for  $q_2$ . Furthermore, the correlation between  $q_2$ , which was indicated to be slightly overfitted, and other CVs is still above 0.94. Therefore, the current hyperparameter tuning framework successfully obtained the RC for the alanine dipeptide isomerization in water, where the DNN models can differ but the important features remain very similar.

### C. On the efficiency of hyperparameter tuning

Since the hyperparameter space defined in the current setup is large, i.e., the number of grids in the nodes and the regularization parameter per node are 50 and 20, respectively, 150 cycles in the Bayesian optimization cannot explore the whole space. It

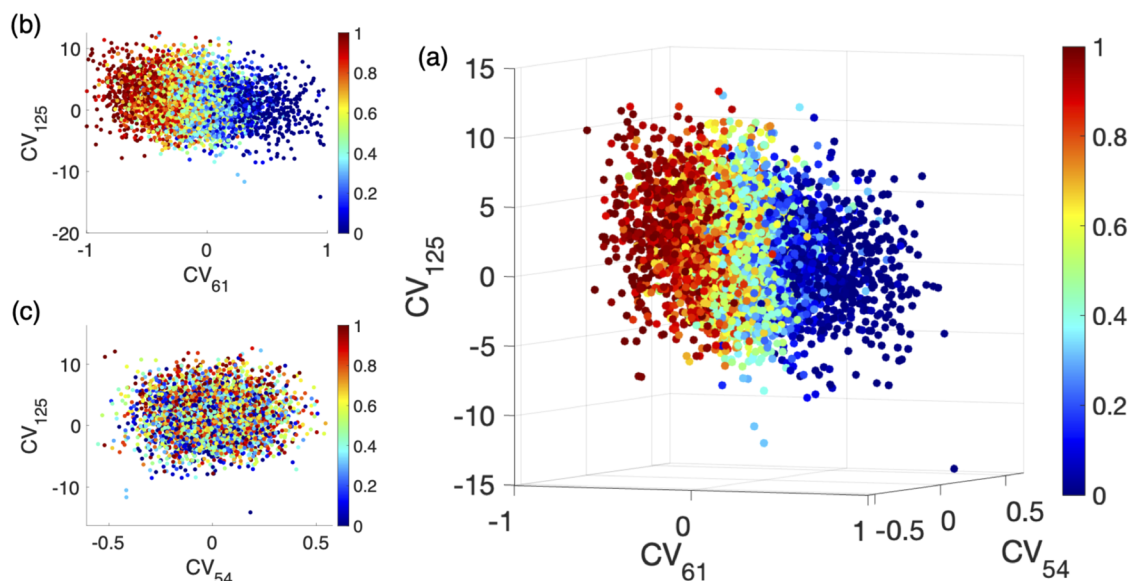


**FIG. 10.** Correlations between the changes in CVs and  $p_B$  in water from the scatter plots in the spaces of (a)  $CV_{61}$  ( $\phi$ ) and  $CV_{125}$  ( $V_{ele}(H_{18})$ ), (b)  $CV_{56}$  ( $\theta$ ) and  $CV_{125}$ , and (c)  $CV_{61}$ ,  $CV_{56}$ , and  $CV_{125}$ . Color range denotes the calculated  $p_B$  at each point.

can thus be anticipated that the diversity in the model is a consequence of insufficient sampling despite each model shows a similar performance.

To this end, we more intensely explored the hyperparameter space for the RCs in water using a fixed number of layers and

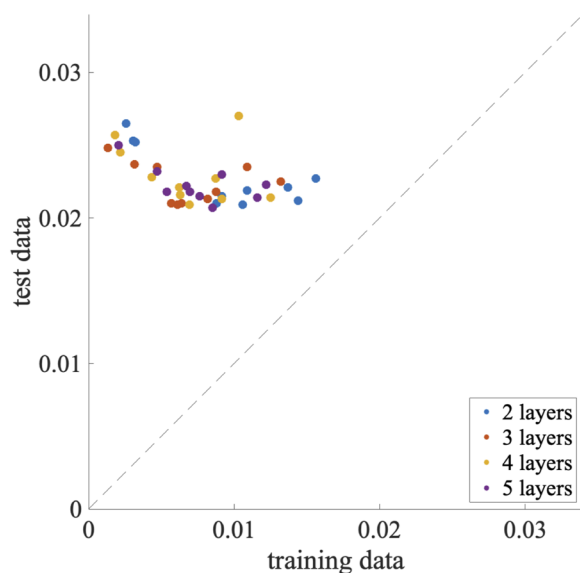


**FIG. 11.** Scatter plot for RMSEs between the predicted and reference  $p_B$  for the training and test datasets where the number of layers is fixed during hyperparameter tuning. Blue, red, yellow, and purple points are from the DNN model with  $N_{layer}$  fixed to 2, 3, 4, and 5, respectively.

500 Bayesian optimization cycles. The optimized hyperparameters for different numbers of fixed layers are summarized in Fig. S10, and the RMSEs for these models are given in Fig. 11. Figure S10 shows that even when the exploration space is restricted and more carefully investigated, the hyperparameters do not converge to a unique value, which confirms that the hyperparameter space is indeed multimodal. The RMSEs for different  $N_{layer}$  in Fig. 11 indicate that the RMSE for the training data tends to improve when the number of layers is increased, whereas the predictability (i.e., RMSE for the test data) does not improve. This may be the reason that  $N_{layer}$  was somewhat smaller in the case of water compared to that in a vacuum. Importantly, the RMSEs in Fig. 11 do not show apparent improvement compared to that with a smaller number of Bayesian trials (Fig. 5). These results show that the current Bayesian optimization of 150 cycles was effective in obtaining the optimal DNN model for the RC from the large number of hyperparameter candidates. The result also highlights that the balance between accuracy (RMSE for training data) and predictability (RMSE for test data) is delicate.

#### IV. SUMMARY

Machine learning approaches have become a powerful tool in determining the RCs from many CV candidates for the reactions in complex environments. DNN is widely used for its effectiveness in taking account of the non-linear contribution of the CVs to the RC, and XAI tools serve as a complement to understand the features that characterize RC, which is otherwise hidden in the complex DNN structure. On the other hand, the structure of the DNN model can be highly flexible, and the hyperparameters that determine the structure are often determined in a non-trivial manner and remain to be a tedious task. Here, we developed the hyperparameter tuning

approach by utilizing the Bayesian optimization method to determine the DNN models for the RC. The DNN model was optimized so as to obtain a RC that can predict the changes of committers from the reactant to product via cross-entropy minimization.

The current approach was first applied to analyze the isomerization of alanine dipeptide in a vacuum. The RC was successfully obtained from ten different initial conditions, where the RMSE of  $p_B$  between the prediction from the RC and the actual data was about 0.005. The correlations between the ten RCs were also very high ( $>0.99$ ). On the other hand, the structure of the optimized DNN model, i.e., the hyperparameters, varied notably between the RCs. By applying the LIME and SHAP methods, all RCs were found to have the same key features, i.e.,  $\phi$  and  $\theta$ . Therefore, despite the apparent differences in the DNN models, all RCs share a common physical mechanism for the reaction in a vacuum with similar accuracy.

This approach was further applied to the isomerization in water. The RC for the reaction in solution was successfully obtained in most cases (9 out of 10), where the RMSEs between the predicted and calculated  $p_B$  for the test data were about 0.02. In one case ( $q_2$ ), we found a slight sign of overfitting, where the committer probability distribution and RMSEs for training and test datasets showed a discrepancy of  $\sim 0.02$  in  $p_B$ . Similarly to the case in a vacuum, the hyperparameters were found to vary notably, but the successfully optimized RCs showed similar  $p_B$ -predictability and high correlation ( $>0.96$ ). By analyzing the RCs using the XAI methods, the RCs were found to have common key features, i.e.,  $\phi$ ,  $\theta$ , and the electrostatic potential from the water on  $H_{18}$ . We note that this solvent contribution to the hydrogen was also found in the torque coordinate proposed previously for the different transition path of the same system.<sup>17</sup> The current RC was able to describe this from a rather simple set of CV candidates while the complex non-linear contribution is taken into account through the DNN model structure. We note that choosing the good CV candidates is important for improving the quality of the RC, such as utilizing the graph neural networks.

The hyperparameter tuning framework was shown to be applicable to explore the RC for reactions in different systems straightforwardly. It is noted that here the RCs were optimized using slightly different datasets, i.e., the same data were partitioned into slightly different training, validation, and test groups due to different random seeds. Even when the same dataset was used, the optimization converged to different optimal when different initial hyperparameters were used (not shown). Therefore, the hyperparameter space of the DNN model for the RC is likely multimodal, and optimization of the hyperparameters can converge to different models with similarly accurate RC depending on the initial conditions. On the other hand, the application of the XAI tools to these different DNN models indicates that suitably optimized DNN models share the same features; therefore, the same mechanism can be extracted from the apparently different DNN models when the hyperparameters are optimized adequately.

## SUPPLEMENTARY MATERIAL

The [supplementary material](#) encompasses a full list of collective variables in vacuum and in water (Table S1), a history of

hyperparameters searched in vacuum (Fig. S1), results for all optimized coordinates in vacuum (Figs. S2–S4), a history of hyperparameters searched in water (Fig. S5), results for all optimized coordinates in water (Figs. S6, S7, and S9), LIME and SHAP analyses without  $q_2$  in water (Fig. S8), a history of hyperparameters searched with a fixed number of layers (Fig. S10), and the structures at about the TS in water (Fig. S11).

## ACKNOWLEDGMENTS

This work was supported by Grant-in-Aid for Scientific Research (Grant Nos. JP22H02035, JP23K23303, JP23KK0254, JP24K21756, JP22H02595, JP22K03550, JP23H02622, JP23K23858, JP23K27313, and JP24H01719) from JSPS. The calculations were partially carried out at the Research Center for Computational Sciences in Okazaki (Grant Nos. 23-IMS-C111, 24-IMS-C051, 24-IMS-C105, and 24-IMS-C198) and using MCRP-M at the Center for Computational Sciences, University of Tsukuba. T.M. also acknowledges the support from the Pan-Omics Data-Driven Research Innovation Center, Kyushu University.

## AUTHOR DECLARATIONS

### Conflict of Interest

The authors have no conflicts of interest to disclose.

### Author Contributions

**Kyohei Kawashima:** Data curation (lead); Formal analysis (lead); Investigation (equal); Methodology (lead); Software (lead); Writing – original draft (lead); Writing – review & editing (equal). **Takumi Sato:** Data curation (equal); Investigation (equal); Software (equal); Writing – review & editing (equal). **Kei-ichi Okazaki:** Funding acquisition (equal); Writing – review & editing (equal). **Kang Kim:** Conceptualization (equal); Funding acquisition (equal); Writing – review & editing (equal). **Nobuyuki Matubayasi:** Funding acquisition (equal); Writing – review & editing (equal). **Toshifumi Mori:** Conceptualization (lead); Funding acquisition (lead); Investigation (lead); Methodology (lead); Project administration (lead); Software (equal); Writing – original draft (lead); Writing – review & editing (lead).

## DATA AVAILABILITY

The data that support the findings of this study are openly available in Zenodo at <https://doi.org/10.5281/zenodo.14378447>.

## REFERENCES

- <sup>1</sup>L. Pauling, “Nature of forces between large molecules of biological interest,” *Nature* **161**, 707–709 (1948).
- <sup>2</sup>R. Wolfenden, “Transition state analogues for enzyme catalysis,” *Nature* **223**, 704–705 (1969).
- <sup>3</sup>V. L. Schramm, “Enzymatic transition state theory and transition state analogue design,” *J. Biol. Chem.* **282**, 28297–28300 (2007).
- <sup>4</sup>L. Jiang, E. A. Althoff, F. R. Clemente, L. Doyle, D. Rothlisberger, A. Zanghellini, J. L. Gallaher, J. L. Betker, F. Tanaka, C. F. Barbas, D. Hilvert, K. N. Houk,

- B. L. Stoddard, and D. Baker, "De novo computational design of Retro-Aldol enzymes," *Science* **319**, 1387–1391 (2008).
- <sup>5</sup>B. Peters, *Reaction Rate Theory and Rare Events* (Elsevier, 2017).
- <sup>6</sup>T. C. Bruice, "A view at the millennium: The efficiency of enzymatic catalysis," *Acc. Chem. Res.* **35**, 139–148 (2002).
- <sup>7</sup>M. Garcia-Viloca, J. Gao, M. Karplus, and D. G. Truhlar, "How enzymes work: Analysis by modern rate theory and computer simulations," *Science* **303**, 186–195 (2004).
- <sup>8</sup>T. Ishida and S. Kato, "Theoretical perspectives on the reaction mechanism of serine proteases: The reaction free energy profiles of the acylation process," *J. Am. Chem. Soc.* **125**, 12035–12048 (2003).
- <sup>9</sup>S. Hayashi, H. Ueno, A. R. Shaikh, M. Umemura, M. Kamiya, Y. Ito, M. Ikeguchi, Y. Komoriya, R. Iino, and H. Noji, "Molecular mechanism of ATP hydrolysis in F<sub>1</sub>-ATPase revealed by molecular simulations and single-molecule observations," *J. Am. Chem. Soc.* **134**, 8447–8454 (2012).
- <sup>10</sup>L. Masgrau and D. G. Truhlar, "The importance of ensemble averaging in enzyme kinetics," *Acc. Chem. Res.* **48**, 431–438 (2015).
- <sup>11</sup>G. Ramachandran and V. Sasisekharan, "Conformation of Polypeptides and Proteins," *Adv. Prot. Chem.* **23**, 283–437 (1968).
- <sup>12</sup>P. L. Geissler, C. Dellago, and D. Chandler, "Kinetic pathways of ion pair dissociation in water," *J. Phys. Chem. B* **103**, 3706–3710 (1999).
- <sup>13</sup>G. Hummer, "From transition paths to transition states and rate coefficients," *J. Chem. Phys.* **120**, 516–523 (2004).
- <sup>14</sup>B. Peters, "Reaction coordinates and mechanistic hypothesis tests," *Annu. Rev. Phys. Chem.* **67**, 669–690 (2016).
- <sup>15</sup>P. G. Bolhuis, C. Dellago, and D. Chandler, "Reaction coordinates of biomolecular isomerization," *Proc. Natl. Acad. Sci. U. S. A.* **97**, 5877–5882 (2000).
- <sup>16</sup>Y. M. Rhee and V. S. Pande, "One-dimensional reaction coordinate and the corresponding potential of mean force from commitment probability distribution," *J. Phys. Chem. B* **109**, 6780–6786 (2005).
- <sup>17</sup>A. Ma and A. R. Dinner, "Automatic method for identifying reaction coordinates in complex systems," *J. Phys. Chem. B* **109**, 6769–6779 (2005).
- <sup>18</sup>B. Peters, G. T. Beckham, and B. L. Trout, "Extensions to the likelihood maximization approach for finding reaction coordinates," *J. Chem. Phys.* **127**, 034109 (2007).
- <sup>19</sup>H. Jung, R. Covino, A. Arjun, C. Leitold, C. Dellago, P. G. Bolhuis, and G. Hummer, "Machine-guided path sampling to discover mechanisms of molecular self-organization," *Nat. Comput. Sci.* **3**, 334–345 (2023).
- <sup>20</sup>S. L. Quaytman and S. D. Schwartz, "Reaction coordinate of an enzymatic reaction revealed by transition path sampling," *Proc. Natl. Acad. Sci. U. S. A.* **104**, 12253–12258 (2007).
- <sup>21</sup>D. Branduardi, F. L. Gervasio, and M. Parrinello, "From A to B in free energy space," *J. Chem. Phys.* **126**, 054103 (2007).
- <sup>22</sup>R. G. Mullen, J.-E. Shea, and B. Peters, "Transmission coefficients, committers, and solvent coordinates in ion-pair dissociation," *J. Chem. Theory Comput.* **10**, 659–667 (2014).
- <sup>23</sup>K.-I. Okazaki, D. Wöhlert, J. Warnau, H. Jung, Ö. Yildiz, W. Kühlbrandt, and G. Hummer, "Mechanism of the electroneutral sodium/proton antiporter PaNhaP from transition-path shooting," *Nat. Commun.* **10**, 1742 (2019).
- <sup>24</sup>T. Mori and S. Saito, "Dissecting the dynamics during enzyme catalysis: A case study of PinI peptidyl-prolyl isomerase," *J. Chem. Theory Comput.* **16**, 3396–3407 (2020).
- <sup>25</sup>Y. Mori, K.-i. Okazaki, T. Mori, K. Kim, and N. Matubayasi, "Learning reaction coordinates via cross-entropy minimization: Application to alanine dipeptide," *J. Chem. Phys.* **153**, 054115 (2020).
- <sup>26</sup>S. Wu, H. Li, and A. Ma, "A rigorous method for identifying a one-dimensional reaction coordinate in complex molecules," *J. Chem. Theory Comput.* **18**, 2836–2844 (2022).
- <sup>27</sup>S. Wu, H. Li, and A. Ma, "Exact reaction coordinates for flap opening in HIV-1 protease," *Proc. Natl. Acad. Sci. U. S. A.* **119**, e2214906119 (2022).
- <sup>28</sup>F. Manuchehrfar, H. Li, W. Tian, A. Ma, and J. Liang, "Exact topology of the dynamic probability surface of an activated process by persistent homology," *J. Phys. Chem. B* **125**, 4667–4680 (2021).
- <sup>29</sup>J. Zhang, O. Zhang, L. Bonati, and T. Hou, "Combining transition path sampling with data-driven collective variables through a reactivity-biased shooting algorithm," *J. Chem. Theory Comput.* **20**, 4523–4532 (2024).
- <sup>30</sup>T. Mori, R. J. Hamers, J. A. Pedersen, and Q. Cui, "An explicit consideration of desolvation is critical to binding free energy calculations of charged molecules at ionic surfaces," *J. Chem. Theory Comput.* **9**, 5059–5069 (2013).
- <sup>31</sup>A. Mardt, L. Pasquali, H. Wu, and F. Noé, "VAMPnets for deep learning of molecular kinetics," *Nat. Commun.* **9**, 5 (2018).
- <sup>32</sup>W. Chen and A. L. Ferguson, "Molecular enhanced sampling with autoencoders: On-the-fly collective variable discovery and accelerated free energy landscape exploration," *J. Comput. Chem.* **39**, 2079–2102 (2018).
- <sup>33</sup>M. M. Sultan and V. S. Pande, "Automated design of collective variables using supervised machine learning," *J. Chem. Phys.* **149**, 094106 (2018).
- <sup>34</sup>J. M. L. Ribeiro, P. Bravo, Y. Wang, and P. Tiwary, "Reweight autoencoded variational Bayes for enhanced sampling (RAVE)," *J. Chem. Phys.* **149**, 072301 (2018).
- <sup>35</sup>J. Rogal, E. Schneider, and M. E. Tuckerman, "Neural-network-based path collective variables for enhanced sampling of phase transformations," *Phys. Rev. Lett.* **123**, 245701 (2019).
- <sup>36</sup>Y. Wang, J. M. L. Ribeiro, and P. Tiwary, "Machine learning approaches for analyzing and enhancing molecular dynamics simulations," *Curr. Opin. Struct. Biol.* **61**, 139–145 (2020).
- <sup>37</sup>L. Bonati, V. Rizzi, and M. Parrinello, "Data-driven collective variables for enhanced sampling," *J. Phys. Chem. Lett.* **11**, 2998–3004 (2020).
- <sup>38</sup>Z. Belkacemi, P. Gkeka, T. Lelièvre, and G. Stoltz, "Chasing collective variables using autoencoders and biased trajectories," *J. Chem. Theory Comput.* **18**, 59–78 (2021).
- <sup>39</sup>L. Bonati, G. Piccini, and M. Parrinello, "Deep learning the slow modes for rare events sampling," *Proc. Natl. Acad. Sci. U. S. A.* **118**, e2113533118 (2021).
- <sup>40</sup>F. Hooft, A. Pérez de Alba Ortiz, and B. Ensing, "Discovering collective variables of molecular transitions via genetic algorithms and neural networks," *J. Chem. Theory Comput.* **17**, 2294–2306 (2021).
- <sup>41</sup>M. Frassek, A. Arjun, and P. G. Bolhuis, "An extended autoencoder model for reaction coordinate discovery in rare event molecular dynamics datasets," *J. Chem. Phys.* **155**, 064103 (2021).
- <sup>42</sup>J. Zhang, Y.-K. Lei, Z. Zhang, X. Han, M. Li, L. Yang, Y. I. Yang, and Y. Q. Gao, "Deep reinforcement learning of transition states," *Phys. Chem. Chem. Phys.* **23**, 6888–6895 (2021).
- <sup>43</sup>T. Kikutsuji, Y. Mori, K.-i. Okazaki, T. Mori, K. Kim, and N. Matubayasi, "Explaining reaction coordinates of alanine dipeptide isomerization obtained from deep neural networks using Explainable Artificial Intelligence (XAI)," *J. Chem. Phys.* **156**, 154108 (2022).
- <sup>44</sup>J. Neumann and N. Schwierz, "Artificial intelligence resolves kinetic pathways of magnesium binding to RNA," *J. Chem. Theory Comput.* **18**, 1202–1212 (2022).
- <sup>45</sup>S. Liang, A. N. Singh, Y. Zhu, D. T. Limmer, and C. Yang, "Probing reaction channels via reinforcement learning," *Mach. Learn.: Sci. Technol.* **4**, 045003 (2023).
- <sup>46</sup>G. Lazzari, H. Jung, P. G. Bolhuis, and R. Covino, "Molecular free energies, rates, and mechanisms from data-efficient path sampling simulations," *J. Chem. Theory Comput.* **19**, 9060–9076 (2023).
- <sup>47</sup>A. N. Singh and D. T. Limmer, "Variational deep learning of equilibrium transition path ensembles," *J. Chem. Phys.* **159**, 024124 (2023).
- <sup>48</sup>D. Ray, E. Trizio, and M. Parrinello, "Deep learning collective variables from transition path ensemble," *J. Chem. Phys.* **158**, 204102 (2023).
- <sup>49</sup>N. Naleem, C. R. A. Abreu, K. Warmuz, M. Tong, S. Kirmizialtin, and M. E. Tuckerman, "An exploration of machine learning models for the determination of reaction coordinates associated with conformational transitions," *J. Chem. Phys.* **159**, 034102 (2023).
- <sup>50</sup>A. Majumder and J. E. Straub, "Machine learning derived collective variables for the study of protein homodimerization in membrane," *J. Chem. Theory Comput.* **20**, 5774–5783 (2024).
- <sup>51</sup>K. Okada, T. Kikutsuji, K.-I. Okazaki, T. Mori, K. Kim, and N. Matubayasi, "Unveiling interatomic distances influencing the reaction coordinates in alanine

dipeptide isomerization: An explainable deep learning approach,” *J. Chem. Phys.* **160**, 174110 (2024).

<sup>52</sup>J. Wu, X.-Y. Chen, H. Zhang, L.-D. Xiong, H. Lei, and S.-H. Deng, “Hyperparameter optimization for machine learning models based on Bayesian optimization,” *J. Elec. Sci. Technol.* **17**, 26–40 (2019).

<sup>53</sup>M. Abadi, A. Agarwal, P. Barham, E. Brevdo, Z. Chen, C. Citro, G. S. Corrado, A. Davis, J. Dean, M. Devin, S. Ghemawat, I. Goodfellow, A. Harp, G. Irving, M. Isard, Y. Jia, R. Jozefowicz, L. Kaiser, M. Kudlur, J. Levenberg, D. Mané, R. Monga, S. Moore, D. Murray, C. Olah, M. Schuster, J. Shlens, B. Steiner, I. Sutskever, K. Talwar, P. Tucker, V. Vanhoucke, V. Vasudevan, F. Viégas, O. Vinyals, P. Warden, M. Wattenberg, M. Wicke, Y. Yu, and X. Zheng, “TensorFlow: Large-scale machine learning on heterogeneous systems” (2015), <https://www.tensorflow.org>.

<sup>54</sup>T. O’Malley, E. Bursztein, J. Long, F. Chollet, H. Jin, L. Invernizzi *et al.* (2019), “Kerastuner,” v.1.4.6, <https://github.com/keras-team/keras-tuner>.

<sup>55</sup>M. T. Ribeiro and S. Singh, in KDD’16: Proceedings of the 22nd ACM SIGKDD International Conference on Knowledge Discovery and Data Mining, 2016.

<sup>56</sup>S. M. Lundberg and S.-I. Lee, “A unified approach to interpreting model predictions,” in *Advances in Neural Information Processing Systems*, 30 (Curran Associates, Inc, 2017).

<sup>57</sup>D. A. Case, K. Belfon, I. Y. Ben-Shalom, S. R. Brozell, D. S. Cerutti, V. W. D. Cruzeiro, T. A. Darden, R. E. Duke, and G. Giambasu, “Amber20” (2020).

<sup>58</sup>A. G. Anderson and J. Hermans, “Microfolding: Conformational probability map for the alanine dipeptide in water from molecular dynamics simulations,” *Proteins: Struct., Funct., Bioinf.* **3**, 262–265 (1988).

<sup>59</sup>R. Salomón-Ferrer, A. W. Götz, D. Poole, S. Le Grand, and R. C. Walker, “Routine microsecond molecular dynamics simulations with AMBER on GPUs. 2. Explicit solvent particle Mesh Ewald,” *J. Chem. Theory Comput.* **9**, 3878–3888 (2013).